Case study

Multi-scale characterization of topographic anisotropy

S.G. Roy [a,*], P.O. Koons [a], B. Osti [a], P. Upton [b], G.E. Tucker [c]

[a] *Earth and Climate Sciences, University of Maine, 111 Bryand Global Science Centre, Orono, ME 04469, United States*
[b] *GNS Science, PO Box 30368, Lower Hutt 5040, New Zealand*
[c] *Cooperative Institute for Research in Environmental Sciences (CIRES) and Department of Geological Sciences, University of Colorado, UCB 399 Boulder, CO 80309-0399, United States*

ABSTRACT

We present the every-direction variogram analysis (EVA) method for quantifying orientation and scale dependence of topographic anisotropy to aid in differentiation of the fluvial and tectonic contributions to surface evolution. Using multi-directional variogram statistics to track the spatial persistence of elevation values across a landscape, we calculate anisotropy as a multiscale, direction-sensitive variance in elevation between two points on a surface. Tectonically derived topographic anisotropy is associated with the three-dimensional kinematic field, which contributes (1) differential surface displacement and (2) crustal weakening along fault structures, both of which amplify processes of surface erosion. Based on our analysis, tectonic displacements dominate the topographic field at the orogenic scale, while a combination of the local displacement and strength fields are well represented at the ridge and valley scale. Drainage network patterns tend to reflect the geometry of underlying active or inactive tectonic structures due to the rapid erosion of faults and differential uplift associated with fault motion. Regions that have uniform environmental conditions and have been largely devoid of tectonic strain, such as passive coastal margins, have predominantly isotropic topography with typically dendritic drainage network patterns. Isolated features, such as stratovolcanoes, are nearly isotropic at their peaks but exhibit a concentric pattern of anisotropy along their flanks. The methods we provide can be used to successfully infer the settings of past or present tectonic regimes, and can be particularly useful in predicting the location and orientation of structural features that would otherwise be impossible to elude interpretation in the field. Though we limit the scope of this paper to elevation, EVA can be used to quantify the anisotropy of any spatially variable property.

© 2015 Elsevier Ltd. All rights reserved.

1. Introduction

Landforms are shaped by the coupled tectonic and climatic processes that drive advection and erosion of rock and transport of sediments. This allows us to make robust interpretations about the geological history of a landscape purely by study of its topography. It is well recognized that the rheological responses of rock to tectonic and topographic stresses determine how strain and associated weakening are partitioned at and below the Earth's surface (Bercovici and Ricard, 2014; Dahlen, 1984; Davis et al., 1983; Koons, 1995; Koons et al., 2012; Montési and Zuber, 2002; Montési, 2004; Upton and Craw, 2014; Upton et al., 2009; Willett et al., 1993; Willett, 1999). The typical rheological response in the upper crust is to localize strain along fault damage zones, which introduces discontinuities in rock strength and uplift relative to baselevel (e.g. Ben-Zion and Sammis, 2003; Faulkner et al., 2010;

Mooney et al., 2007; Sammis et al., 1986; Sibson, 1977). Further still, the planar geometry and orientation of fault damage zones are grossly predictable based on the tectonic stress field (Coulomb, 1773; Enlow and Koons, 1998; Terzaghi, 1944). Tectonic strain therefore introduces directionally dependent characteristics of rock displacement and damage, both of which influence the pace of geomorphic responses (Molnar et al., 2007; Roy et al., 2015). As a result, drainage network patterns often reflect the underlying anisotropy of fault damage zones, whereas in the absence of strain, drainage network patterns are largely isotropic (Roy et al., 2015).

By measuring topographic anisotropy, or the directional dependence of landforms, from the scale of valleys and ridges to entire basins and orogens, we can make an assessment of the magnitude and orientation of past or present tectonic strain fields across multiple length scales. Our approach is to create and utilize an every-direction variogram analysis (EVA) technique to quantify topographic anisotropy by calculating elevation variance at multiple scales and in multiple directions from any point on a surface. Our goal is to make useful first-order interpretations of how topography contains multiscale, spatially dependent information about past and present tectonic strain

conditions using a simple parallel code written in the CUDA language (Wilt, 2013). Specifically, we use EVA on landforms with distinct patterns of anisotropy associated with tectonic strain, river incision, and/or sediment deposition, in order to establish a generalized model for linking the topographic fabric to its formative process. Several synthetic landscapes and natural landscapes from New Zealand are featured in order to test the versatility of our method. We then compare EVA to the self-affine power law scaling method, a popular method for examining the directional dependent and fractal properties of landscapes (Dodds and Rothman, 2000; Sung and Chen, 2004; Xu et al., 1993), in order to understand how these two methods differ in sensitivity to directional dependent landscape fabrics. We conclude with a short discussion on possible future uses and improvements to EVA.

2. Every-direction variogram analysis (EVA)

2.1. Statistical method

There is no single method of classification that will adequately characterize and compare the spatial distribution of directional dependence. Some have characterized directional dependence by drawing correlations between the orientations of streams and bedrock joints (e.g. Ericson et al., 2005; Judson and Andrews, 1955), while others have made useful qualitative descriptions of drainage patterns with respect to strength and uplift gradients and thresholds (e.g. Lubowe, 1964; Zernitz, 1932). Watershed hypsometry (e.g. Lifton and Chase, 1992; Walcott and Summerfield, 2008) and directional dependent fractal analysis (e.g. Sung and Chen, 2004) have recently become useful tools for interpreting the influence of spatially variable conditions. Still others have used sinuosity or tortuosity to determine the directional dependence of individual rivers and their correlation to structural features (e.g. Hack and Young, 1959; Roy et al., 2015). However, these methods provide limited information about the spatial distribution or directionality of anisotropy, are often limited to a single spatial scale, or they do not fully represent all components of the landscape. For this reason we explore the directional and scale dependencies of topography using the variance of elevation along a surface (Kitanidis, 1997; Koons et al., 2012; Trevisani et al., 2009). EVA is an
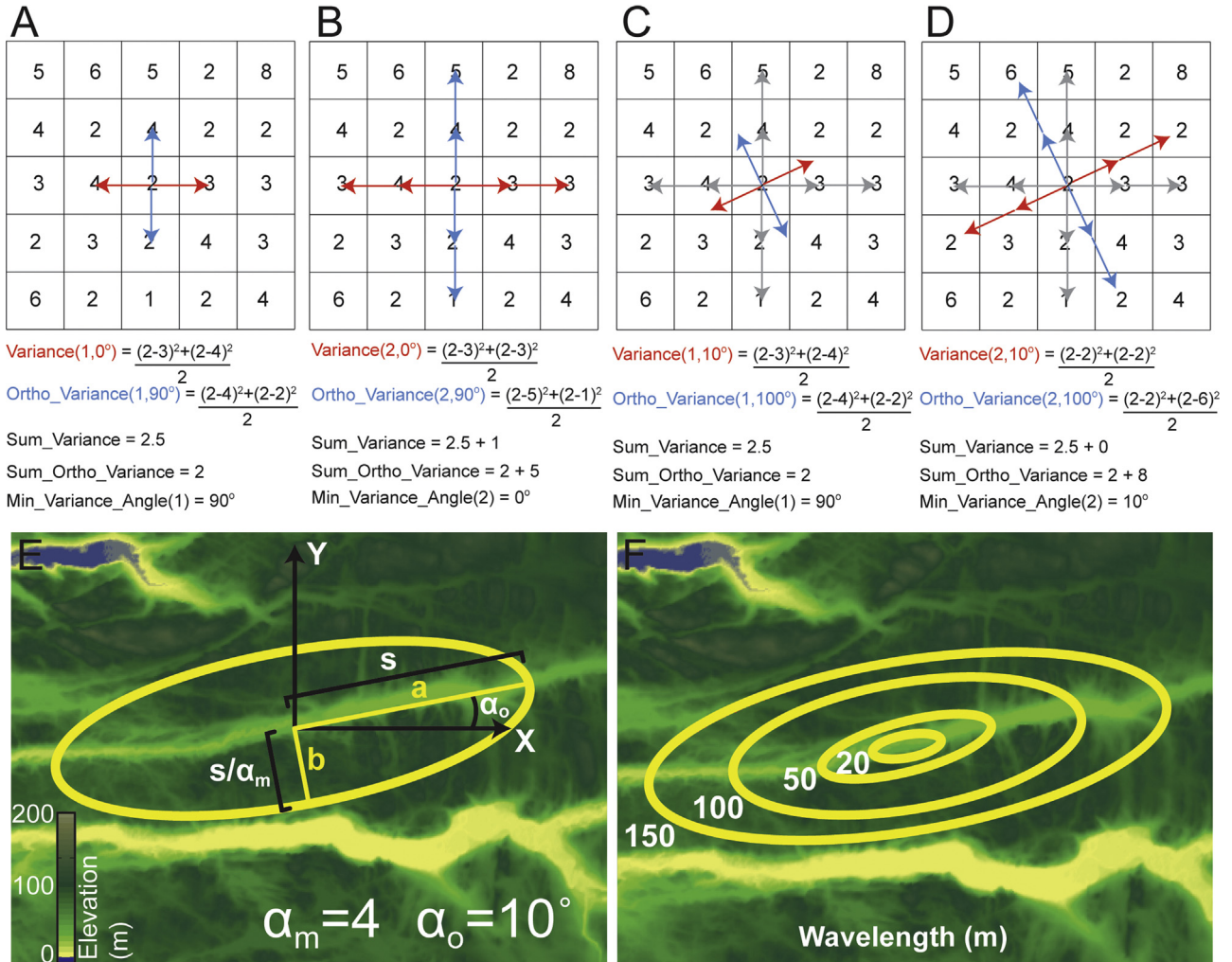

Fig. 1. (A) An example grid in which we apply our variance algorithm. Starting at $\varphi = 0°$ with separation distance equal to the grid resolution, calculate variance between center point and points 0° and 180° and separation distance 1 away from center (red arrows). Also calculate variance for points orthogonal to 0° and 180° (blue arrows). (B) Separation distance is doubled and variance values are calculated for the new scale. The variance for this scale is the average of the new variance and the variance calculated at the previous separation distance. (C) Variance is now measured for $\varphi = 10°$, 190° and $s = 1$. The new variance value does not exceed the previously calculated value at the given scale and is therefore not used to measure anisotropy. (D) The calculation is repeated at the second scale, variance is less than the previous calculation and so is now used to measure anisotropy for $s=2$. (E) An example of anisotropic topography. Anisotropy magnitude α_m is taken by dividing the minimum variance from the variance value measured at a perpendicular angle. Anisotropy orientation α_o is equal to the orientation of minimum variance. Ellipses: the semi-major axis equals scale, the semi-minor axis equals the ratio of scale and anisotropy magnitude. The orientation of the semi-major axis is equal to α_o. (F) The orientation and magnitude of anisotropy is measured over multiple scales. The size of the ellipse represents the scale over which anisotropy is measured. (For interpretation of the references to color in this figure legend, the reader is referred to the web version of this article.)
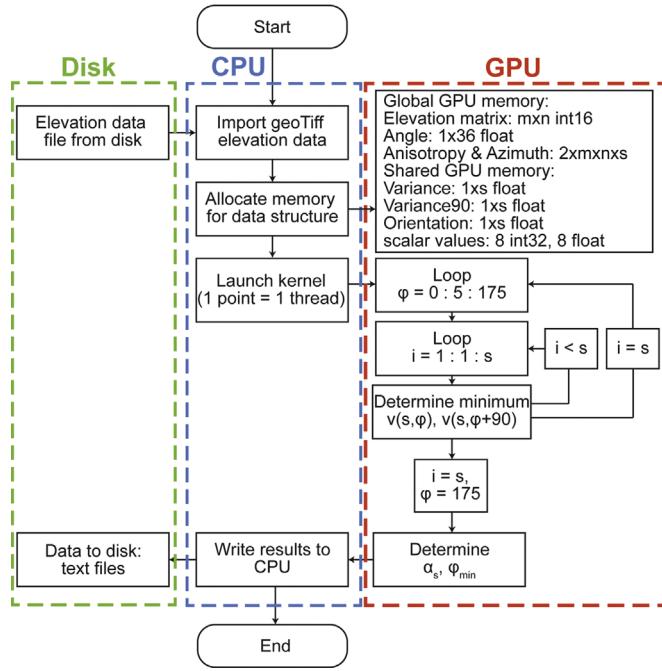
Fig. 2. Flow chart for the EVA algorithm.

improvement on previous variogram methods because elevation variance is calculated between multiple points at multiple scales and multiple directions, leading to a rich quantitative determination of anisotropy magnitude and orientation at multiple scales for every point on a landscape. We measure variance v^2 using the statistical method.

$$v^2(x, y) = [z(x, y) - z(x + \Delta x, y + \Delta y)]^2 \tag{1}$$

where $z(x, y)$ is the elevation at a point with coordinates x, y, and $z(x + \Delta x, y + \Delta y)$ is the elevation at a point with a separation distance, or length scale, equal to $\Delta x, \Delta y$ using a 2D Cartesian coordinate system (Fig. 1A). The second point is found using the least squares method. In order to measure directional dependence we must calculate variance over multiple separation distances and directions within a large population of elevation data. Separation distance s is a length scale equal to or greater than the spatial resolution of topographic data. Divided into Cartesian components:

$$\Delta x = s \cos \varphi,$$
$$\Delta y = s \sin \varphi \tag{2}$$

where φ is the angle between the two points, taken at 5° intervals for our analysis. For simplicity we average variance in opposing directions, assuming that directional dependence is symmetric (Fig. 1A). Variance is also averaged over separation distance in order to reduce the signal of small scale features over long separation distances

$$v^2(x, y, s, \varphi) = \frac{1}{2s} \sum_{i=1}^{s} [v^2(i, \varphi) + v^2(i, \varphi + 180)] \tag{3}$$

where $v^2(x, y, s, \varphi)$ is the variance, averaged along all separation distances $i = 1$ to s for angles φ and $\varphi + 180$ (Fig. 1B) at location x,y. In other words, $v^2(x, y, s, \varphi)$ represents the average variance over all separation distances up to and including s for one orientation at one location. The minimum variance for every separation distance and its respective angle are recorded in addition to the variance values orthogonal to the minimum values (Fig. 1C, D). We define

anisotropy as the ratio between these two variance values

$$\alpha_m(s, x, y) = \frac{v_c^2 + v^2(s, \varphi_{min} + 90)}{v_c^2 + v^2(s, \varphi_{min})},$$

$$\alpha_o(s, x, y) = \varphi_{min} \tag{4}$$

where $\alpha_m(s, x, y)$ is anisotropy magnitude measured at multiple separation distances at location x,y, $\alpha_o(s, x, y)$ is the anisotropy orientation equal to φ_{min}, the angle of minimum variance for separation distance s at location x,y, and v_c^2 is equal to the variance of the relative vertical error estimate of the dataset ($v_c^2 = 36 \text{ m}^2$ for SRTM3 data, $v_c^2 = 100 \text{ m}^2$ for SRTM30 data) used to diminish extreme variance sensitivity at the smallest scales that could be attributed to error (Rabus et al., 2003). The anisotropy can then be used to quantitatively interpret the directional dependence of elevation at a single point (Fig. 1E), for multiple scales (concentric ellipses in Fig. 1F), or multiple points on a surface, which we discuss in Section 3. This method can be used to quantify the anisotropy of any spatially variable parameter, but we limit the scope of this paper to elevation.

2.2. Computational method for generating anisotropy maps with EVA

The statistical method mentioned above is deployed in parallel for CUDA, a C-based programming model developed by NVIDIA to accelerate the execution time of numerous parallel statistical calculations by taking advantage of a Graphical Processing Unit (GPU) (Wilt, 2013). The elevation files read by EVA contain elevation data in meters for coordinates in degree decimal units at an isotropic resolution of 30″ for Sections 3.1.6 and 3″ for all other examples. Data are generally in integer format, imported from Geotiff files, but EVA can also accept float format. All of the elevation data are used for the calculation, but anisotropy is only calculated for points that are at least separation distance s away from the boundaries of the elevation data due to the lack of data beyond the spatial limits. For every point, anisotropy is measured over a scale interval covering three orders of magnitude. Data processing follows the flow chart in Fig. 2. First, the integer values of elevation are extracted from the elevation data file and stored in a C matrix. Then the matrices and variables required in the CPU and the GPU are initialized. A CUDA kernel is then launched such that each point in the matrix containing the elevation data is a thread. The data passed to the kernel are the elevation matrix and the angle array that contains angles in five-degree intervals from 0 to 175. For each of the threads in the GPU the code loops through the scales to calculate variance for all angles in the angle array and determines the anisotropy magnitude and orientation for that particular scale. At the end of the kernel for each (x,y) point in the elevation data matrix, magnitude and orientation values are produced for all scales and these values are transferred to the CPU where they can be saved to disk.

2.3. Methods for delivering anisotropy data

Using the equations above the magnitude and direction of the anisotropy can be quantified at any scale and any point on a landscape. This information can become difficult to visualize in a meaningful way, so we choose to pursue a three-stage method for delivering anisotropy data from EVA.

I. First, we create simplified landforms that resemble our natural examples, and use EVA to measure anisotropy at a single point on each surface. We do this in order to understand the basic shape of anisotropy produced by the process that builds that characteristic shape.

II. Second, after we have determined the basic pattern of anisotropy from the simple surfaces, we perform the same analysis on the natural landscape example. The position of the point used for this analysis should be similar to the point measured in stage one to validate a comparison. In both cases we use multiple ellipses to represent anisotropy at multiple scales (see Fig. 1F).

III. Third, we use EVA to calculate anisotropy data for all points on the landscape in order to fully represent the regional topographic fabric and the spatial variations found within. The analysis of multiple points enhances our ability to see local changes in anisotropy that could otherwise become lost in the average topographic fabric or misrepresented by a single point analysis. The use of thousands of ellipses is prohibitive for this multipoint analysis, so we plot two different colors representing the magnitude and orientation of anisotropy for a single scale at every point. The use of color to represent the orientation and magnitude of anisotropy is not
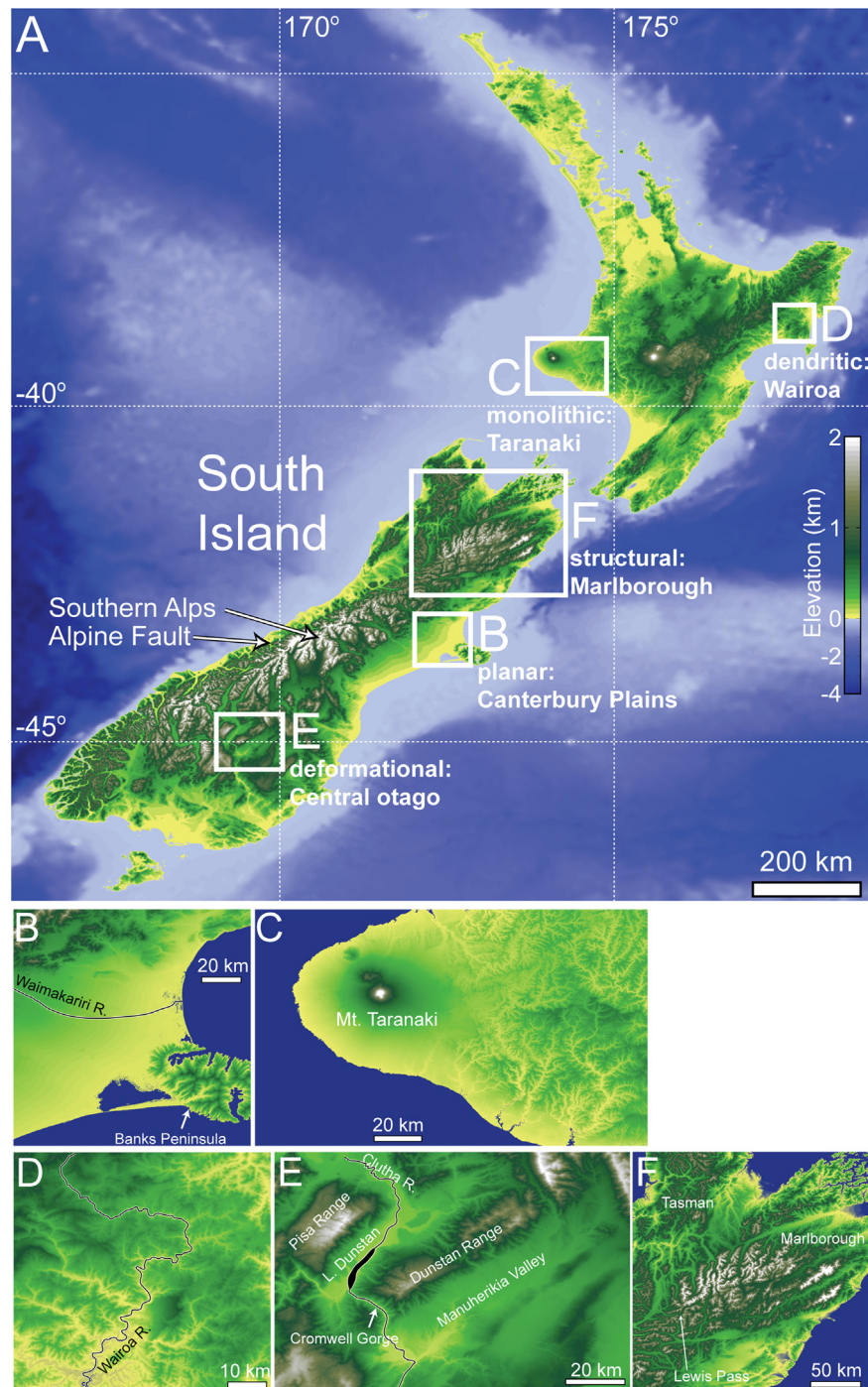

Fig. 3. Topographic maps of (A) New Zealand and the regions of (B) Canterbury Plains, (C) Taranaki, (D) Wairoa, (E) Central Otago, and (F) Marlborough. These locations are used for further analysis in Section 3.1. Map A uses topographic data from the SRTM30 mission (~1 km resolution) and bathymetric data from the ETOPO1 mission (~2 km resolution). Maps B–F use topographic data from the SRTM3 mission (~90 m resolution) (Rabus et al., 2003). Please note scale change between maps and the difference in scale between bathymetric and terrestrial elevation data in map A.

unlike electron backscatter diffraction maps produced for interpretation of crystallographic preferred orientations (Dingley, 2004; Schwarzer et al., 2009).

3. Topographic fabric in New Zealand

We use field locations in New Zealand for our statistical analysis of topographic anisotropy. The Southern Alps of New Zealand (Fig. 3A) are an orogenic mountain range wrought from the oblique collision of the Australian and Pacific tectonic plates. Uplift of crust relative to the regional baselevel has produced a mountain range with a directional dependence dictated by the orientation of the Alpine Fault (e.g. Koons, 1994, 1990; Little et al., 2005; Norris and Cooper, 1995; Norris et al., 1990; Sutherland, 1999) and rheological variations along strike (Upton and Craw, 2014; Upton et al., 2009), which can generate a fold-thrust topography (Jackson et al., 1996) (Fig. 3E). Within the Southern Alps, typically at length
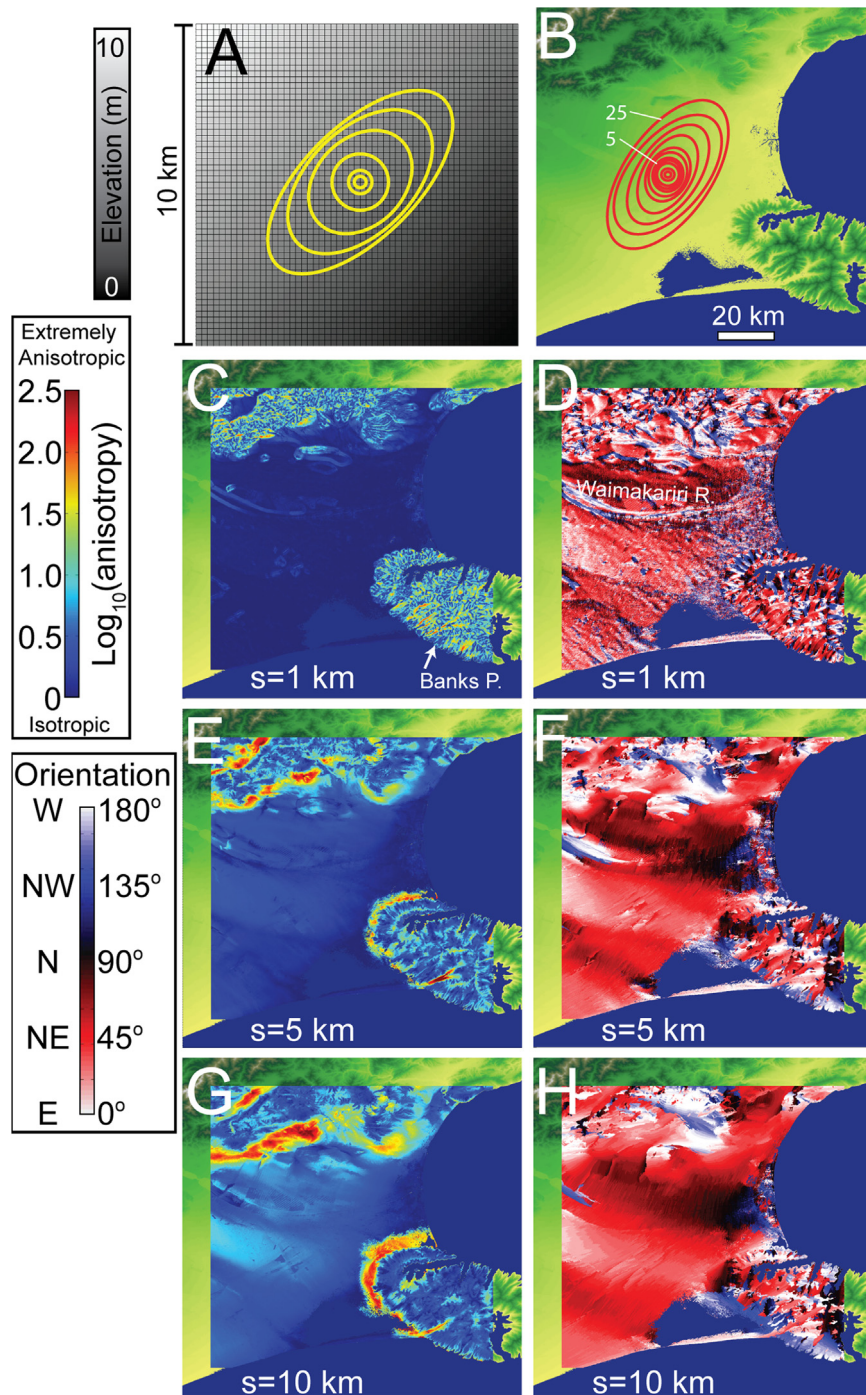

Fig. 4. (A) Plane gently dipping southeast; a simplified replication of low relief planar topography found in Canterbury Plains. Greyscale: black is low, white is high elevation for this and all following synthetic examples. Anisotropy of single point represented by concentric ellipses for this and all following figures (see Fig. 1E,F; yellow or red color used based on visibility). Numbers represent the scale in kilometers for the indicated ellipses. (B) Anisotropy measured at single point in center of Canterbury Plains alluvial fan (red ellipses). See Fig. 3A for elevation color scale for this and all following natural examples. Anisotropy measured up to maximum scale of 25 km. (C) Anisotropy magnitude and (D) orientation map at 1 km, (E, F) 5 km, and (G, H) 10 km scale. Color scales for both map types on left are used for this and all following figures. (For interpretation of the references to color in this figure legend, the reader is referred to the web version of this article.)

scales of 20 km or less (Koons, 1995, 1994; Koons et al., 2012), patterns of deformation and rock damage in fault structures influence the position and erosive power of streams and rivers as they incise into the uplifting orogen. The largest rivers in the Marlborough district are influenced by damage and deformation along major active tectonic structures, represented by a strong northeast trending orientation of ridges and valleys (Craw et al., 2008; Wilson et al., 2004) (Fig. 3F). Conversely, the Wairoa River cuts a dendritic drainage pattern as it incises into a largely homogeneous and uniformly uplifted erodible siltstone (Crosby and Whipple, 2006) (Fig. 3D). Sediments course through drainage networks in the Southern Alps and some deposit in the large alluvial fan of the Canterbury Plains region (Fig. 3B) (Leckie, 1994). On the North Island, volcanism has led to the creation of isolated, monolithologic stratovolcanoes, such as Mt. Taranaki (Fig. 3C), that provide a simple, well-defined form with steep slopes (Grant-Taylor, 1964; Harrison and White, 2004).

3.1. EVA results: anisotropy maps

We apply EVA to the planar (Canterbury Plains, Fig. 4), isolated peak (Mt. Taranaki, Fig. 5), dendritic (Wairoa, Fig. 6), deformational (Central Otago, Fig. 7), and fault damage and deformation (Marlborough, Fig. 8) topographic patterns of New Zealand, as well as a larger scale analysis of the entire South Island (Fig. 9). However, we begin each example by analyzing simplified topographic shapes that resemble the natural examples in order to gain insight into the basic patterns of topographic anisotropy characteristic to each example, as explained in Section 2.3. Our reasons for choosing each simplified topographic shape are described below. Topographic anisotropy was mapped in the natural examples from 0.1–10 km for the local examples and 1–200 km for the South Island example.

3.1.1. Planar example-Canterbury Plains

Planar topographic patterns offer minimal topographic relief over kilometer length scales. In Canterbury Plains, New Zealand, large amonts of alluvium have deposited to form an alluvial fan gently dipping to the southeast (Leckie, 1994) (Fig. 3B). We replicate the flat, gently dipping form of large fan deposits in our synthetic landscape by considering a flat plane with a low dip angle (Fig. 4A). Variance tends to be relatively low in all directions due to the lack of relief, represented by circular, generally equant ellipses at short length scales (Fig. 4A). Anisotropy does increase with greater separation distance along the contour of the plane because variance persistently approaches zero perpendicular to the slope while values steadily increase parallel to slope. For a horizontal planar surface, the signal would be isotropic at all
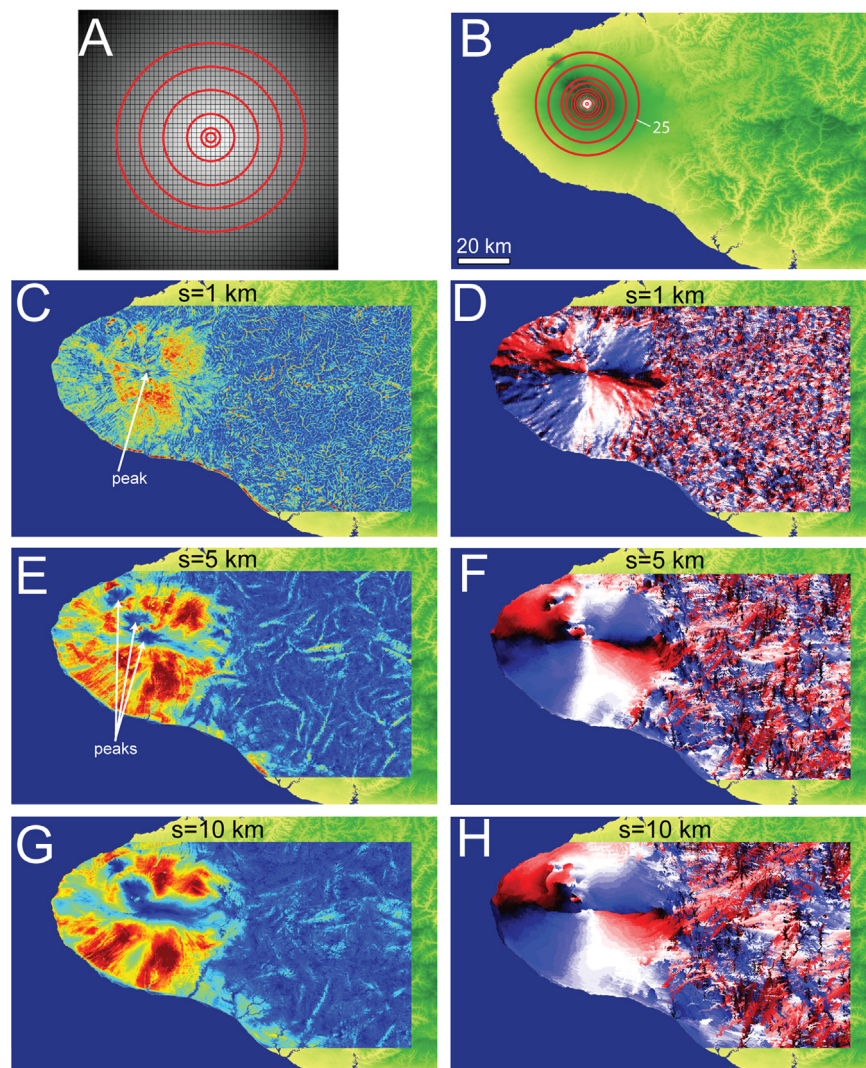

Fig. 5. (A) Idealized, steep cone; a simplified replication of isolated stratovolcano Mt. Taranaki. (B) Anisotropy measured at single point at peak of Mt. Taranaki. Anisotropy measured up to maximum scale of 25 km. (C) Anisotropy magnitude and (D) orientation map at 1 km, (E, F) 5 km, and (G, H) 10 km scale.
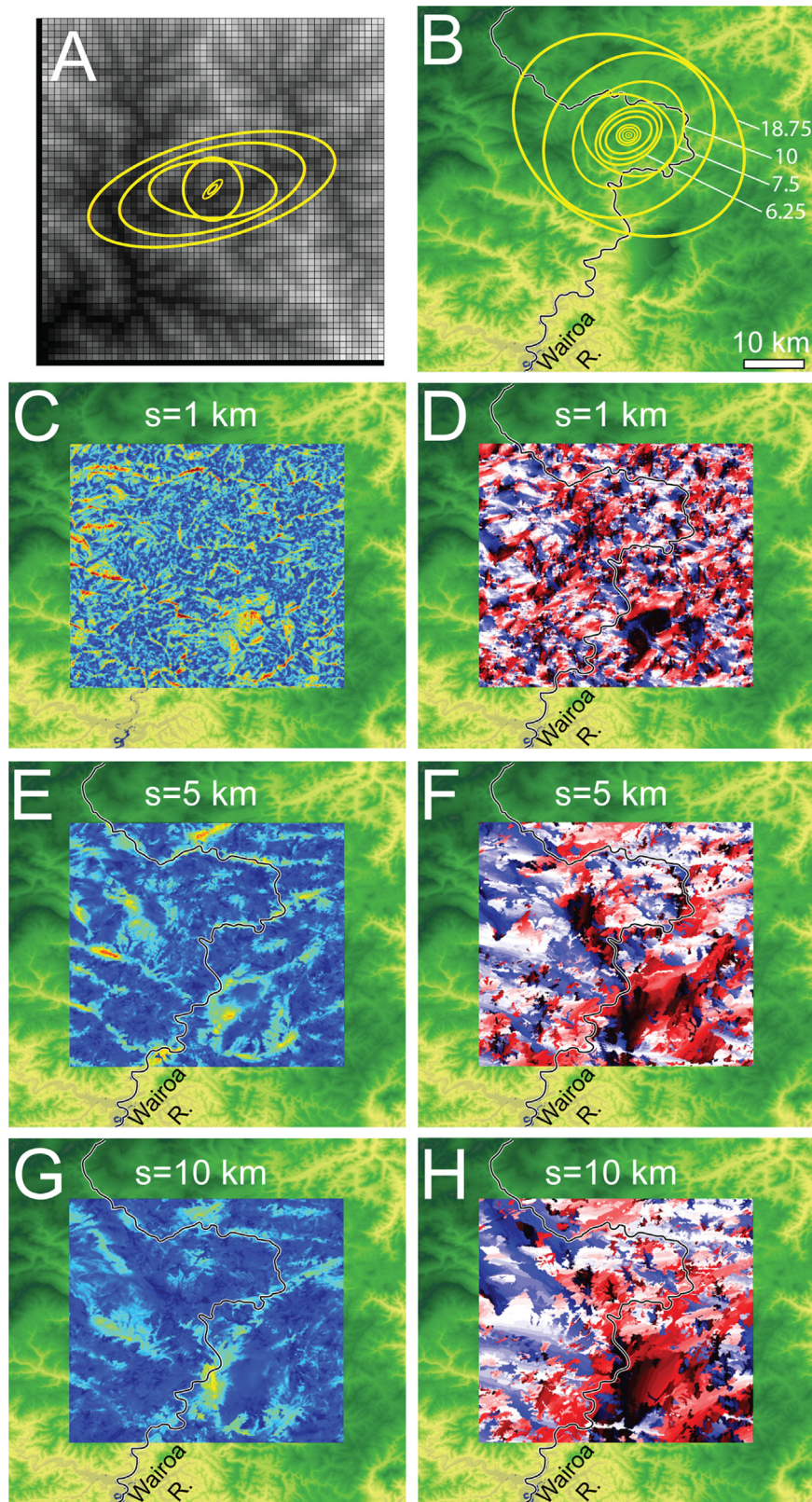
Fig. 6. (A) Dendritic surface created from a stream power-based landscape evolution model created on a uniform substrate. (B) Anisotropy measured at single point in Wairoa region. Anisotropy measured up to maximum length scale of 18.75 km. (C) Anisotropy magnitude (Eq. (4)) and (D) orientation map at 1 km, (E, F) 5 km, and (G, H) 10 km scale.

scales. The degree of anisotropy is proportional to the surface gradient. The natural example follows a similar trend but shows slight changes in orientation associated with small, kilometer scale lateral changes in surface slope (Fig. 4B).

The 1 km scale pattern displays homogeneous isotropy across the Canterbury Plains, in agreement with the single point analysis (Fig. 4C). The plains are dominantly isotropic but there is a small degree of anisotropy and orientation change associated with the
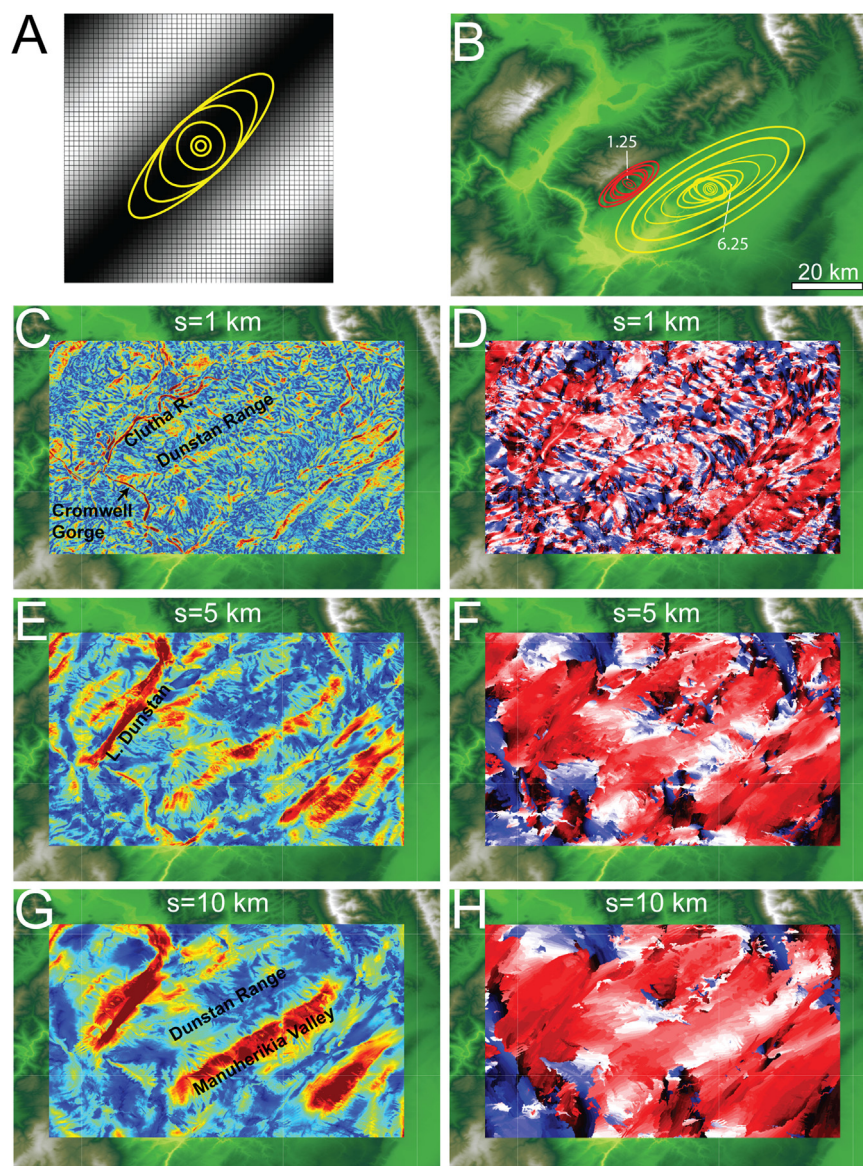
Fig. 7. (A) Sine wave surface used as a simplified replication of synform–antiform pairs found in Central Otago. (B) Anisotropy measured at two points in Manuherikia River Valley (yellow) and the secondary gorge (red). Numbers represent the scale in kilometers for the indicated ellipses. Anisotropy measured up to maximum scale of 25 km in the valley, 7.5 km in the gorge. (C) Anisotropy magnitude and (D) orientation map at 1 km, (E, F) 5 km, and (G, H) 10 km scale. (For interpretation of the references to color in this figure legend, the reader is referred to the web version of this article.)

Waimakariri River and small local hills and ridges. Orientation on the plains is more variable but there is a small majority of northeast trending data points south of the Waimakariri River (Fig. 4D). Outside of the plains the pattern of anisotropy reflects a ridge and valley topography associated with fluvial incision, particularly visible on Banks Peninsula. Anisotropy in the plains is slightly greater at 5–10 km scales, and orientation is parallel to the general northeast strike of the gently sloping surface (Fig. 4E–H). The steep topography along the Southern Alps to the northwest and the Banks Peninsula to the southeast create a spike in anisotropy along the perimeters in the plains (Fig. 4G).

3.1.2. Isolated peak example-Taranaki

We replicate the shape of an isolated stratovolcano in our synthetic landscape by considering a cone shape with maximum elevation centered on the surface (Fig. 3C, Fig. 5A). Unlike the previously discussed topographic pattern, isolated peaks are persistently isotropic at all scales because variance is extremely high in all directions from the peak, as can be seen in the the concentric

equant ellipses of Fig. 5A. Mt. Taranaki dominates its regional topographic field as an isolated feature of high relief and is represented by the same pattern of radial isotropy (Fig. 5B).

Anisotropy maps display a strong signal of isotropy about the peak, closely surrounded by a radially oriented distribution of extremely high magnitude anisotropy at all scales (Fig. 5C–H). The slopes of the stratovolcano increase in anisotropy magnitude at greater scale, but their orientation remains relatively unchanged. Changes in anisotropy magnitude along the slopes reveal the imperfect symmetry of the stratovolcano and the presence of two other extinct and largely incised stratovolcanoes trending northwest (Grant-Taylor, 1964). Anisotropy is particularly low at the peaks of the extinct volcanoes and along the eastern flank of Mt. Taranaki. To the east of Mt. Taranaki relief is largely influenced by fluvial processes and anisotropy in that region is greatest at the 1 km scale. Anisotropy on Mt. Taranaki is greatest at 10 km scale and could become greater at scales we do not measure here.
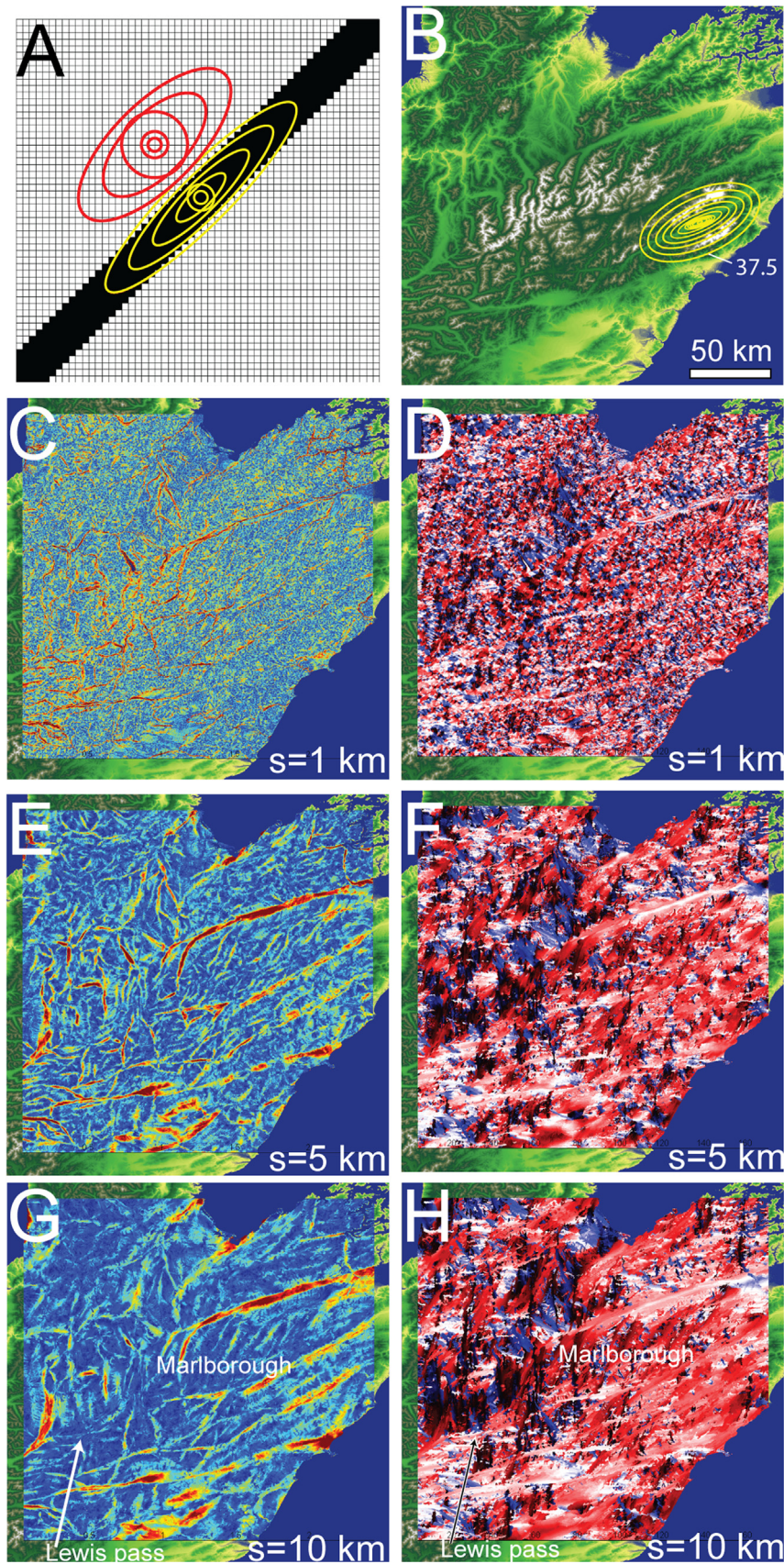
Fig. 8. (A) Low relief trough bisecting high relief plateau; a simplified replication of fault damage influenced topography. (B) Anisotropy measured at single point in Marlborough. Anisotropy measured up to maximum scale of 37.5 km. (C) Anisotropy magnitude and (D) orientation map at 1 km, (E, F) 5 km, and (G, H) 10 km scale.
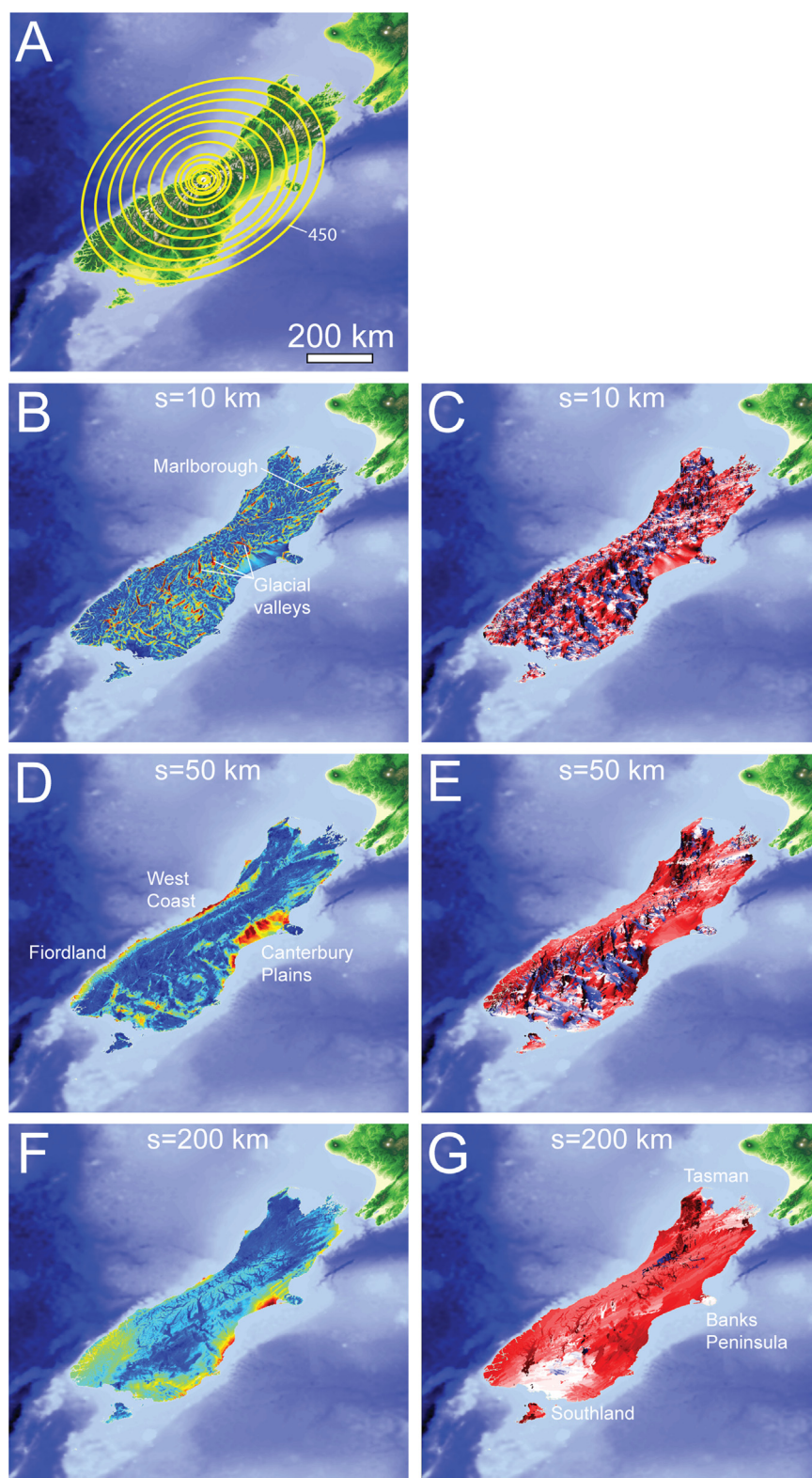
Fig. 9. (A) Anisotropy measured at single point near Southern Alps divide. Anisotropy measured up to maximum scale of 450 km. (B) Anisotropy magnitude and (C) orientation map at 10 km, (D, E) 50 km, and (F, G) 200 km scale.

3.1.3. Dendritic example-Wairoa

Dendritic fluvial networks can display significant relief, but directional dependence may vary significantly with the variable scale of river meanders (Fig. 3D). We replicate the dendritic shape of the Wairoa River by using the landscape evolution model CHILD, in order to create a surface with idealized, homogeneous surface conditions

(Fig. 6A) (Tucker et al., 2001). This model generated surface is the product of stream power-controlled erosion of a uniform substrate under uniform environmental and geomorphic conditions, in which the rate of uplift is steadily matched by the rate of erosion. Surface runoff exits the model through a single outlet point in order to provide one large river network for analysis.

Changes in orientation are common over multiple spatial scales in the synthetic experiment (Fig. 6A). Anisotropy measurements are taken at a specific point located on a low order channel just before confluence with a higher order channel. At a scale up to 0.4 km, anisotropy is dominated by the low order channel, but at the 1 km scale the high order channel begins to influence anisotropy, and it eventually dominates at longer scales. Meandering rivers and streams in the Wairoa District of New Zealand display a similar spectrum of anisotropy magnitude and orientation from the reference of a single point (Fig. 6B). In this natural case there are four significant shifts in orientation for the range of length scales considered (6.25–18.75 km). Anisotropy magnitude is greatest at short scales, before the first large shift in orientation (below 6.25 km), but wanes at longer scales as the orientation of dendritic channels become less consistent.

The Wairoa region hosts a mélange of anisotropy at a short scale, in agreement with the single point analyses above. Anisotropy magnitude (Fig. 6C) and orientation (Fig. 6D) are highly variable across sub-kilometer distances. Anisotropy is greatest at 1 km scale (Fig. 6C–G). There are some cases where anisotropy persists at 10 km scale along the large ridges separating higher order channels, otherwise the topography becomes generally isotropic (Fig. 6G). At 5–10 km scale, there is a broad divide between an average west-northwest orientation on the west side of the Wairoa River and an east-northeast trend on the eastern side (Fig. 6F, H). To the south, the Wairoa River valley generally trends to the north-northeast.

3.1.4. Deformational example-Central Otago

The deformational signal in topography is associated with tectonic strain from differential plate motion. Central Otago is characterized by widely distributed deformation caused by tectonic strain in a weak lower crust (Upton et al., 2009). Limited rainfall in this region ($\sim$200 mm a^{-1} (Tomlinson and Sansom, 1994)) has helped to preserve the antiform-synform pairs associated with this type of deformation (Fig. 3E). This topographic pattern is also similar to the fold-thrust belts of the Appalachian and Zagros Orogens (Chapple, 1978; Tucker and Slingerland, 1996; Williams and Hatcher, 1982). We replicate the fold-thrust pattern formed in Central Otago with a simple sinusoidal ridge and trough geometry (Fig. 7A). At a point chosen at the trough of the synthetic waveform, the anisotropy increases with scale and orientation remains parallel to the fold axis (Fig. 7C, E, and G).

We measure anisotropy at two points in Central Otago: one in the Manuherikia River valley (Fig. 3E; large yellow ellipses, Fig. 7B), and one in a secondary gorge on the Dunstan Range (Fig. 3E; red ellipses, Fig. 7B). As expected from the synthetic example, the fold axis-parallel trend in anisotropy exists at both locations, but only beyond a scale of 6.25 km at Manuherikia River Valley and 1.25 km in the secondary gorge. Below these scales, both locations exhibit a northwest trend that matches the trend of small gorges, ravines, and streams, but opposes the general northeast orientation of the synform–antiform pairs and the larger rivers. Anisotropy magnitude increases with scale for both cases.

At a scale of 1 km, anisotropy is strongest along the reach of the Clutha River and the anisotropy signal is dominated by rivers, streams, and ravines (Fig. 7C). The Clutha River follows the axis of a synform valley to the north but crosses the Dunstan Range through Cromwell Gorge (Fig. 3E), which follows the active River Channel Fault (Thomson, 1993). Orientation is spatially variable at the 1 km scale (Fig. 7D), dominated by streams that incise into the antiform ridges and generally trend orthogonal to the fold axis. At greater length scales (Fig. 7E–G), anisotropy orientations begin to follow the fold axes of the antiform–synform pairs and the anisotropy signal begins to increase along the fold axes of the synform basins. The Clutha River anisotropy signal is mostly

diminished at this longer scale except for where it follows the axis of the synform basin at Lake Dunstan. Anisotropy along the antiform ridges has a somewhat uniform orientation at the 10 km scale but a much lower anisotropy compared to the synform basins.

3.1.5. Fault damage and deformation example-Marlborough

Topographic patterns associated with fault damage suggest rapid erosion of faults, fractures, and other mechanical defects in the crust (e.g. Becker et al., 2014; Ericson et al., 2005; Koons, 1994; Koons et al., 2012; Molnar et al., 2007; Roy et al., 2015; Scheidegger, 1979). We replicate the shape of fault erosion and uplift in our synthetic landscape by considering a narrow, linear trough of low elevation in a plateau of high elevation (Fig. 8A). This simplified pattern is used to highlight the isolated effect of erosion along a fault zone. The ridge and valley fabric associated with drainages confined or influenced by fault damage leads to extreme local anisotropy in the form of long, anomalously straight river reaches (Fig. 8A). Ridges that separate the eroded fault zones are wider and exhibit the same directional dependence but with lower magnitude anisotropy.

The region of Marlborough, New Zealand (Fig. 3F) hosts a series of nearly vertically dipping NE trending strike-slip faults associated with pervasive distributed strain in the lower crust (Craw et al., 2008; Wilson et al., 2004). However, there is also a component of shortening perpendicular to fault strike that has led to orogenesis (Van Dissen and Yeats, 1991). For this reason the topographic shape of Marlborough cannot be attributed completely to erosion dictated by fault damage, but the drainage network pattern in this region does appear to reflect the Marlborough Fault System. Based on EVA results, anisotropy is greatest in the large river valleys that coincide with large fault zones in a way that is similar to the synthetic example (Fig. 8B).

Anisotropy magnitude remains extremely high and orientation persists at longer scales along the anomalously straight valleys (Fig. 8C–H). The small tributaries that incise into the valley walls and ridges influence the topographic fabric at the 1 km scale, producing a locally pronounced signal of anisotropy with an orientation roughly orthogonal to the large rivers draining northeastward (Fig. 8D). From 1 km to 5 km scale, topographic orientation in ridges and valley walls tends to align with the large rivers, shifting in an east-northeast direction, particularly in eastern and southern Marlborough (Fig. 8F). In Western Marlborough and around Lewis Pass, the dominant orientation becomes north-northwest following other valleys that correlate with other fault structures (Craw et al., 2013). There is a significant decrease in anisotropy magnitude in ridges and valley walls at greater scale, coinciding with the change in orientation (Fig. 8G, H). In the western part of the Marlborough region, erosion along intersecting faults causes segmentation of ridges, further reducing ridge anisotropy.

3.1.6. Larger scale example-south island, New Zealand

Fig. 9A is an example of EVA used to measure the directional dependence of a single point on the Southern Alps at separation distances up to 450 km. There is an obvious topographic anisotropy in the South Island associated with the trend of the Southern Alps that initially increases, then persists with greater scale. This single point analysis is apparently insensitive to more diverse landforms, some of which were explored above, that appear at shorter scales and in other locations (Fig. 3A).

The characteristic patterns of these shorter scale landforms are revealed with anisotropy maps covering all of South Island (Fig. 9B–G, please also see supplementary Animations S1 and S2). Bathymetric data were used to calculate anisotropy for terrestrial points, but anisotropy was not measured for any bathymetric

points. Topographic anisotropy magnitude and orientation were measured from 1 km to 200 km for all points on South Island. At 10 km scale, anisotropy is greatest in the eastern glacial valleys of the Southern Alps and along the river valleys in the Marlborough region (Fig. 9B, C). Orientations are diverse but follow the local directions of ridges and valleys. At 50 km scale, the edges of the Southern Alps, particularly the west coast, Fiordland, and Canterbury Plains, exhibit high magnitude anisotropy while anisotropy in the glacial valleys is diminished (Fig. 9D, E). The orientation data in these regions generally follow the northeast trend of the Southern Alps. At 200 km scale, anisotropy increases along the Southern Alps divide, and the orientation data are dominated by the trend of the orogen except in Central Southland, Banks Peninsula, and Tasman regions (Fig. 9F, G).

4. Discussion

4.1. Generalized landform fabrics

The five types of landforms that we explore (dendritic, deformational, fault damage, planar, and isolated peak) host unique patterns of anisotropy associated with the processes that shaped them and their initial form. In general, tectonic activity can introduce and amplify anisotropy at any scale (please refer to supplementary Table S1 and supplementary Fig. S1 for more information). At the orogenic scale (> 100 km scale), tectonism dominates the topographic fabric of New Zealand by controlling the gross shape of the Southern Alps (Fig. 9A). The orogen is the product of oblique collision and so is a deformational landform under our characterization. Below the orogenic scale, the shape of topography, and hence anisotropy, is dependent on fluvial and glacial processes reflecting the presence or absence of tectonic deformation and/or damage gradients.

Regions that lack past or present tectonism or consist of a uniform lithology and climate, and simple initial form, are often nearly isotropic. Homogeneous landscapes do not provide a directionally dependent advantage for rivers, and hence a dendritic drainage pattern is the common result. River meanders can occur at a multitude of scales and as a result, topographic anisotropy gradually decreases and orientation frequently changes with increasing scale. For this reason dendritic landforms commonly exhibit high anisotropy magnitude with sporadic orientation at short scales and low anisotropy magnitude with sporadic orientation at large scales. This is the case for the Wairoa region, in which a largely homogeneous and highly erodible siltstone unit is uniformly uplifted and incised by a dendritic river network (Fig. 6). A similar case is made for the region east of Mt. Taranaki (Fig. 5), where anisotropy magnitude reaches a local maximum at 1 km, similar to the average scale of river meanders. Based on our analysis, dendritic rivers in New Zealand are typically limited to less than 10 km scale, indicating that tectonic deformation and damage begin to dominate at length scales of 10 km or greater.

The tectonic signature of large anisotropy persists at shorter scales through the introduction of damage and differential uplift along fault structures and the strong sensitivity of fluvial processes to these heterogeneous changes. This is the case for Central Otago (Fig. 7), in which drainage patterns align with the distributed deformation of a fold-thrust belt (Jackson et al., 1996), and in Marlborough (Fig. 8), in which a combination of localized deformation and fault damage (Wilson et al., 2004) is also reflected by the straight ridge-valley topography. In both cases, rivers conform to the heterogeneous damage and displacement fields, causing high order rivers to align with fold basin axes or fault structures. Anisotropy in deformational landforms is best preserved in alluvium-filled fold basins, as seen in the 5 km and 10 km scales in Central Otago (Fig. 7E–H) and at the 50 km scale in Canterbury Plains (Fig. 4D, E). Conversely, fault damage landforms depend on fluvial incision along faults to produce their characteristically extreme multiscale anisotropy. However, topography in the Marlborough region is likely attributed to a combination of deformation and river incision along fault structures.

Ridges host much lower anisotropy magnitude than fold basins and structurally aligned valleys, due to fluvial incision by short, low order tributaries that convene at an angle orthogonal to structures and fold axes. The presence of these tributaries causes a shift in anisotropy orientation and a sharp change in magnitude in ridges at a scale generally equal to half of the ridge width, assuming that ridge relief is symmetric (Fig. 7B). For our natural examples this anisotropy shift often occurs between 1 and 10 km. The synthetic landscapes in Figs. 7A and 8A fail to replicate this scale-dependent shift in the ridge because they lack fluvial contributions to topography. In the case of Marlborough, ridge width is a function of the fault spacing width (Fig. 8). In the case of Central Otago, ridge width is a function of crustal rheology and the thickness of the deforming layer (Chapple, 1978; Upton et al., 2009). As a consequence, ridge anisotropy contains important quantitative information about scale-dependent interactions between crustal rheology and the drainage network pattern in Central Otago (e.g. Jackson et al., 1996). In both cases, these ridge and valley landforms are apparent at scales equal to or less than 50 km according to our South Island-scale analysis (Fig. 9), and 30 km according to other analyses of New Zealand topography (Koons, 1995, 1994; Koons et al., 2012).

Coastal depositional processes tend to create a wide distribution of low relief and consequently exhibit low anisotropy on their own, but this pattern is commonly punctuated by the edges of the basin in which they are located. This is the case for Canterbury Plains (Fig. 4), in which a large alluvial fan maintains a consistent gentle slope towards the sea. Large rivers may have a small local effect on anisotropy, but in general the weak contour-parallel anisotropy pattern is pervasive. This pattern abruptly changes when the length scale is long enough to reach the edge of the basin containing the alluvial fan, at which point there is a significant increase in anisotropy at an orientation parallel to the edge of the basin. Fig. 4G displays the sharp change in anisotropy magnitude associated with the edges of the basin, and high magnitude values in the Canterbury Plains at longer scales (Fig. 9D) indicate that at scales equal to or greater than 50 km, measurements of anisotropy become more representative of topography in the larger scale fold basin containing the alluvial fan rather than the fan itself.

Isolated peaks are characterized by an isotropic signal at their peak surrounded by concentric high anisotropy along the slopes and a radial pattern of orientation, which persists across all measured length scales in our analysis. However, this generalization breaks down slightly for Mt. Taranaki (Fig. 5) due to asymmetric fluvial incision along the flanks of the volcano and the presence of two nearby smaller cones that diminish the symmetry along the flanks of the stratovolcano.

4.2. Comparison of EVA to self-affine power law scaling

Over the past ~45 years a large body of work has demonstrated that many systems can be described as self-similar, meaning that specific patterns become statistically invariant across multiple scales (e.g. Barnsley et al., 1988; Jébrak, 1997; Klinkenberg and Goodchild, 1992; Mandelbrot, 1967; Roy et al., 2012), or self-affine, meaning the scale-invariant behavior is apparent but limited by directional dependence (Dodds and Rothman, 2000; Sung and Chen, 2004; Xu et al., 1993). We have already recognized directional dependence in our examples, therefore we would like to compare EVA results with a test for self-affinity.

Measurements of variance in elevation may tend to increase as a power law function with increasing length scale

$$v^2(s) = ks^\sigma \tag{5}$$

where $v^2(s)$ is the variance at separation distance, or scale s, σ is the scaling parameter, and k is equal to $v^2(1)$. Unlike in Eq. (3), variance is not averaged over the separation distance. For a truly self-affine system the scaling parameter, generally a value between 0 and 1, remains constant and contains information about the complexity or roughness of a topographic surface (Chase, 1992; Klinkenberg and Goodchild, 1992; Lifton and Chase, 1992; Shepard et al., 1995). A larger scaling parameter symbolizes greater variance, or surface complexity, with increasing scale. A fractal dimension can be calculated from the scaling parameter (Klinkenberg and Goodchild, 1992; Lifton and Chase, 1992; Shepard et al., 1995; Sung and Chen, 2004; Wilson and Dominic, 1998), but we choose to use the scaling parameter on its own as a diagnostic index of landscape complexity.

We first test the self-affine method on a single, randomly chosen point in Central Otago (Fig. 3E, Fig. 7) and measure variance for separation distances up to 9 km in 360 directions in 1° intervals (Fig. 10A). There is an obvious spread in data owing to the directionally dependent roughness of the landscape. By sampling a greater number of points and averaging variance by orientation (Fig. 10B), an apparent power law distribution emerges for all orientations within our range of separation distances. The scaling parameter and the coefficient both vary as a function of orientation. The lowest scaling parameter of 0.52 occurs along 36°, east-northeast, which happens to be virtually parallel to the fold axes in Central Otago (Fig. 10C). The largest scaling parameter of 0.74 occurs along 124°, north-northwest, virtually orthogonal to the dominant ridge orientation.

These results are suggestive of a distinct fabric that is pervasive throughout the sampled region, with a more complex fabric that exists orthogonal to the main ridge-valley orientation, and less complexity parallel to it. In this way the basic fabric of the landscape is recognized by this analysis and is in agreement with EVA. Despite this result, it is clear that this method is not sensitive to the spatial dependence of topographic fabric. The need to average variance values over 960,000 points spanning a 9600 km² area in order to generate the expected power-law distribution diminishes the information about local changes in fabric. Additionally, the need to average variance across large areas to produce the expected power-law trend is not necessarily a self-affine characteristic and it may be inappropriate to analyze the landscape by such a statistical method (Clauset and Shalizi, 2007).

EVA affords us a better understanding of topographic fabric by being sensitive to spatial, scale-dependent changes in topographic anisotropy. It is not possible to obtain this resolution by confining the results to regional-scale analysis using the self-affine scaling parameter, which is limited by either lack of directional data or lack of spatial relevance, depending on how data are averaged. In Central Otago, the location- and scale-dependent shift in anisotropy orientations associated with fluvial incision and tectonic deformation precludes this type of terrain from analysis by scale-independent, self-affine statistics. Using EVA we are able to more completely determine and characterize the scale dependencies that arise when multiple mechanisms contribute to landscape formation.

4.3. Future work

Our method and analysis illustrate the strength of topographic anisotropy in determining and disseminating the scale-dependent contributions of tectonic and erosional processes. Our code allows
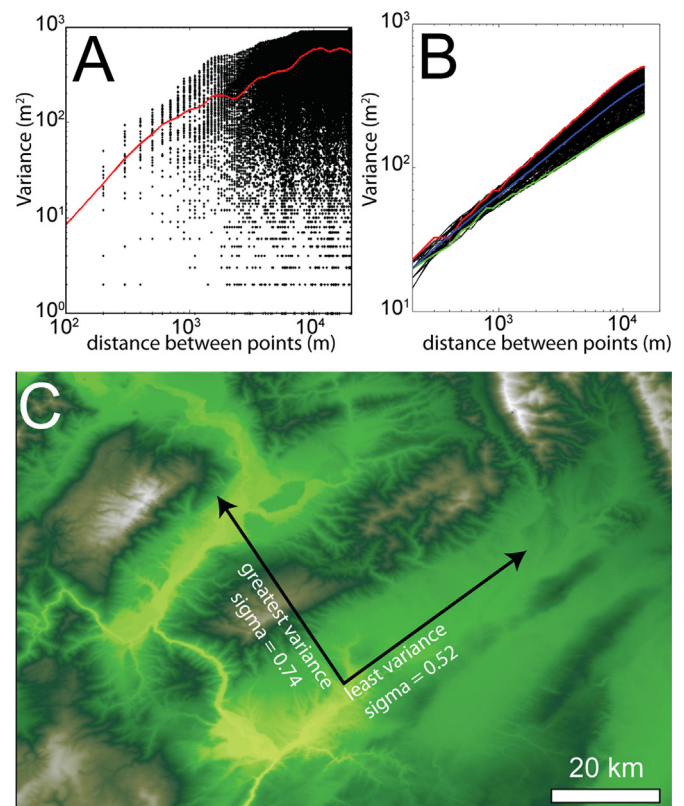

Fig. 10. (A) variance measured at single, randomly chosen point along 1° intervals for 360° up to 20 km separation distance at ~100 m intervals. Black dots indicate the variance, red line indicates trend of the averaged data. (B) Plot similar to A but for all points in the domain, variance values are averaged by direction to compare scaling by orientation. Maximum scaling parameter indicated in red (0.74), minimum indicated in green (0.52), mean indicated in blue. (C) Map of Central Otago with the maximum and minimum scaling parameter orientations indicated. (For interpretation of the references to color in this figure legend, the reader is referred to the web version of this article.)

for the rapid calculation of variograms for every direction and each point on a surface for multiple scales. The next step would be to use EVA to interpret the topographic record of past and present changes in climate and tectonics. We have only explored generalized landscape patterns associated with specific processes, which can be expanded upon by studying a larger sampling of less generalizable landforms, and pursuing more situations in which several processes, occurring at different times or simultaneously, have created an integrated landform that does not reflect a single generalizable shape. For example, changes in drainage density attributed to changes in climate may influence the scale at which fabric transition occurs. Also, changes in tectonic regime will potentially introduce new deformational and structural features with new anisotropy. The dissemination of tectonic landscape features may ultimately indicate patterns of mantle advection at depth, while an understanding of tectonic controls on rates and processes of landscape evolution could produce information on the timing of tectonic events. The persistence and complexity of anisotropic signals depends on how the tectonic strain field evolves with time: new tectonic regimes can overprint the original topographic signal, or the signal can slowly recede as tectonism halts.

Another possibility is to use EVA to explore topographic anisotropy that is not associated with tectonic activity. For example, it would be possible to use EVA to find the edges of paleoshorelines, or to quantify lithological controls on topography that are not specifically related to tectonism. EVA can be used for any spatially variable characteristic, so there are applications beyond elevation variance. The potential for unearthing the geological history of an

area purely from topographic form is an old concept, and the utilization of multiscale EVA may significantly increase the capabilities of these first-order interpretations of landforms.

5. Conclusions

We apply multiscale every-direction variograms analysis (EVA) to quantify the fabric of landscapes with diverse landforms over a range of spatial scales. Topographic anisotropy, defined as the ratio of minimum variance to the orthogonal variance, is found to be a useful metric for linking generalized landforms to their influential tectonic and fluvial processes. We apply this method in a multiscale approach to help interpret scale-dependent changes in topographic fabric. Generally speaking, fluvial processes tend to reduce anisotropy while tectonic processes tend to increase anisotropy. Depositional environments, such as alluvial fans and basins, are largely isotropic but increase in anisotropy at longer scales due largely to boundary effects near the edge of basins. Landscapes shaped by fault erosion tend to host extremely high anisotropy magnitude across multiple scales and in uniform orientations. Deformational landforms increase in anisotropy magnitude at greater length scales. Isolated stratovolcanoes are generally isotropic at their peaks with strong radial anisotropy along the surrounding flanks. Other methods for determining topographic fabric such as self-affine power law statistics provide useful information but may lack the sensitivity to spatial and directional fabrics that reveal the relative contributions of tectonics and climate. Further work on this topic should focus on a greater extent of testing upon more landforms with ambiguous or variable tectonic, climatic, and geomorphological histories.

Acknowledgments

Appendix A. Supplementary material

Supplementary data associated with this article can be found in the online version at http://dx.doi.org/10.1016/j.cageo.2015.09.023.

References

Barnsley, M.F., Devaney, R.L., Mandelbrot, B.B., Peitgen, H.-O., Saupe, D., Voss, R.F., 1988. The Science of Fractal Images. Springer-Verlag, New York.

Becker, R.A., Tikoff, B., Riley, P.R., Iverson, N.R., 2014. Preexisting fractures and the formation of an iconic American landscape: Tuolumne Meadows, Yosemite National Park, USA. GSA Today 24, 4–10.

Ben-Zion, Y., Sammis, C., 2003. Characterization of fault zones. Pure Appl. Geophys. 160, 677–715.

Bercovici, D., Ricard, Y., 2014. Plate tectonics, damage and inheritance. Nature 508, 513–516.

Chapple, W.M., 1978. Mechanics of thin-skinned fold-and-thrust belts. Geol. Soc. Am. Bull. 89, 1189–1198.

Chase, C.G., 1992. Fluvial landsculpting and the fractal dimension of topography. Geomorphology 5, 39–57.

Clauset, A., Shalizi, C.R., 2007. Power-Law Distributions in Empirical Data, Santa Fe Institute Working Paper.

Coulomb, C., 1773. Essai sur une application des règles de maximis & minimis à

quelques problèmes de statique, relatifs à l'architecture. Mem. Acad. Roy. Div. Sav. 7, 343–387.

Craw, D., Burridge, C.P., Upton, P., Rowe, D.L., Waters, J.M., 2008. Evolution of biological dispersal corridors through a tectonically active mountain range in New Zealand. J. Biogeogr. 35, 1790–1802.

Craw, D., Upton, P., Horton, T., Williams, J., 2013. Migration of hydrothermal systems in an evolving collisional orogen, New Zealand. Miner. Depos. 48, 233–248.

Crosby, B.T., Whipple, K.X., 2006. Knickpoint initiation and distribution within fluvial networks: 236 waterfalls in the Waipaoa River, North Island, New Zealand. Geomorphology 82, 16–38.

Dahlen, Fa, 1984. Noncohesive critical Coulomb wedges: an exact solution. J. Geophys. Res. 89, 10125–10133.

Davis, D., Suppe, J., Dahlen, F.A., 1983. Mechanics of fold-and-thrust belts and accretionary wedges. J. Geophys. Res. 88, 1153–1172.

Dingley, D., 2004. Progressive steps in the development of electron backscatter diffraction and imaging microscopy. J. Microsc. 213, 214–224.

Dodds, P.S., Rothman, D.H., 2000. Scaling, universality, and geomorphology. Annu. Rev. Earth Planet. Sci. 28, 571–610.

Enlow, R., Koons, P.O., 1998. Critical wedges in three dimensions: Analytical expressions from Mohr-Coulomb constrained perturbation analysis. J. Geophys. Res. 103, 4897–4914.

Ericson, K., Migon, P., Olvmo, M., 2005. Fractures and drainage in the granite mountainous area: a study from Sierra Nevada, USA. Geomorphology 64, 97–116.

Faulkner, D.R., Jackson, C.A.L., Lunn, R.J., Schlische, R.W., Shipton, Z.K., Wibberley, C.A.J., Withjack, M.O., 2010. A review of recent developments concerning the structure, mechanics and fluid flow properties of fault zones. J. Struct. Geol. 32, 1557–1575.

Grant-Taylor, T.L., 1964. Volcanic history of Western Taranaki. N. Z. J. Geol. Geophys 7, 78–86.

Hack, J.T., Young, R.S., 1959. Intrenched meanders of the north fork of the Shenandoah River, Virginia. Geol. Surv. Prof. Pap, 354-A.

Harrison, A.J., White, R.S., 2004. Crustal structure of the Taupo Volcanic Zone, New Zealand: stretching and igneous intrusion, Geophys. Res. Lett. p. 31.

Jackson, J., Norris, R., Youngson, J., 1996. The structural evolution of active fault and fold systems in central Otago, New Zealand: evidence revealed by drainage patterns. J. Struct. Geol. 18, 217–234.

Jébrak, M., 1997. Hydrothermal breccias in vein-type ore deposits: a review of mechanisms, morphology and size distribution. Ore Geol. Rev. 12, 111–134.

Judson, S., Andrews, G., 1955. Pattern and form of some valleys in the driftless area, Wisconsin. J. Geol. 63, 328–336.

Kitanidis, P.K., 1997. Introduction to Geostatistics: Applications in Hydrogeology, 1st ed. Press Syndicate of the University of Cambridge, Cambridge, UK.

Klinkenberg, B., Goodchild, M.F., 1992. The fractal properties of topography: a comparison of methods. Earth Surf. Process. Landf. 17, 217–234.

Koons, P.O., 1990. Two-sided orogen: collision and erosion from the sandbox to the Southern Alps, New Zealand. Geology 18, 679–682.

Koons, P.O., 1994. Three-dimensional critical wedges: tectonics and topography in oblique collisional orogens. J. Geophys. Res. 99, 12,301–12,315.

Koons, P.O., 1995. Modeling the topographic evolution of collisional belts. Annu. Rev. Earth Planet. Sci. 23, 375–408.

Koons, P.O., Upton, P., Barker, A.D., 2012. The influence of mechanical properties on the link between tectonic and topographic evolution. Geomorphology 137, 168–180.

Leckie, D.A., 1994. Canterbury Plains, New Zealand-implications for sequence stratigraphic models. Am. Assoc. Pet. Geol. Bull. 78, 1240–1256.

Lifton, N., Chase, C., 1992. Tectonic, climatic and lithologic influences on landscape fractal dimension and hypsometry: implications for landscape evolution in the San Gabriel Mountains, California. Geomorphology 5, 77–114.

Little, T.A., Cox, S., Vry, J.K., Batt, G., 2005. Variations in exhumation level and uplift rate along the oblique-slip Alpine fault, central Southern Alps, New Zealand. Geol. Soc. Am. Bull. 117, 707–723.

Lubowe, J.K., 1964. Stream junction angles in the dendritic drainage pattern. Am. J. Sci. 262, 325–339.

Mandelbrot, B.B., 1967. How long is the coast of Britain? Statistical self-similarity and the fractal dimension. Science (80-.) 156, 636–638.

Molnar, P., Anderson, R.S., Anderson, S.P., 2007. Tectonics, fracturing of rock, and erosion. J. Geophys. Res. 112, F03014.

Montési, L., Zuber, M., 2002. A unified description of localization for application to large-scale tectonics. J. Geophys. Res. Solid Earth, 107.

Montési, L.G.J., 2004. Controls of shear zone rheology and tectonic loading on postseismic creep. J. Geophys. Res. 109, B10404.

Mooney, W., Beroza, G., Kind, R., 2007. Fault zones from top to bottom: a geophysical perspective. In: Handy, M., Hirth, G., Hovius, N. (Eds.), Tectonic Faults Agents of Change on a Dynamic Earth. MIT Press, Cambridge, MA, USA, pp. 24–61.

Norris, R.J., Cooper, A.F., 1995. Origin of small-scale segmentation and transpressional thrusting along the Alpine Fault, New Zealand. Geol. Soc. Am. Bull. 107, 231–240.

Norris, R.J., Koons, P.O., Cooper, A.F., 1990. The obliquely-convergent plate boundary in the South Island of New Zealand: implications for ancient collision zones. J. Struct. Geol. 12, 715–725.

Rabus, B., Eineder, M., Roth, A., Bamler, R., 2003. The shuttle radar topography mission—a new class of digital elevation models acquired by spaceborne radar. ISPRS J. Photogramm. Remote Sens. 57, 241–262.

Roy, S.G., Johnson, S.E., Koons, P.O., Jin, Z., 2012. Fractal analysis and thermal-elastic

modeling of a subvolcanic magmatic breccia: the role of post-fragmentation partial melting and thermal fracture in clast size distributions. Geochem. Geophys. Geosyst. 13, Q05009.

Roy, S.G., Koons, P.O., Upton, P., Tucker, G.E., 2015. The influence of crustal strength fields on the patterns and rates of fluvial incision. J. Geophys. Res. Earth Surf. 120, 275–299.

Sammis, C.G., Osborne, R.H., Anderson, L., Banerdt, M., White, P., 1986. Self-similar cataclasis in the formation of fault gouge. Pure Appl. Geophys. 124, 53–78.

Scheidegger, A.E., 1979. The principle of antagonism in the Earth's evolution. Tectonophysics 55, T7–T10.

Schwarzer, R.A., Field, D.P., Adams, B.L., Kumar, M., Schwartz, A.J., 2009. Present State of Electron Backscatter Diffraction and Prospective Developments. In: Schwartz, A.J., Kumar, M., Adams, B.L., Field, D.P. (Eds.), Electron Backscatter Diffraction in Materials Science. 2nd ed. Springer, New York.

Shepard, M.K., Brackett, R.A., Arvidson, R.E., 1995. Self-affine (fractal) topography: surface parameterization and radar scattering. J. Geophys. Res. 100, 11709–11718.

Sibson, R.H., 1977. Fault rocks and fault mechanisms. J. Geol. Soc. London. 133, 191–213.

Sung, Q.-C., Chen, Y.-C., 2004. Self-affinity dimensions of topography and its implications in morphotectonics: an example from Taiwan. Geomorphology 62, 181–198.

Sutherland, R., 1999. Cenozoic bending of New Zealand basement terranes and Alpine Fault displacement: a brief review. New Zeal. J. Geol. Geophys. 42, 295–301.

Terzaghi, K. von, 1944. Theoretical Soil Mechanics.

Thomson, R., 1993. Clyde Dam Engineering Geological Completion Report Volume 1: Text and Appendices.

Tomlinson, A.I., Sansom, J., 1994. Rainfall normals for New Zealand for the period 1961 to 1990. NIWA Sci. Technol., Wellington, New Zealand, Ser. Number 3.

Trevisani, S., Cavalli, M., Marchi, L., 2009. Variogram maps from LiDAR data as fingerprints of surface morphology on scree slopes. Nat. Hazards Earth Syst. Sci. 9, 129–133.

Tucker, G., Lancaster, S., Gasparini, N., 2001. The channel-hillslope integrated landscape development model (CHILD). In: Harmon, R.S., Doe, W.W. (Eds.), Landscape Erosion and Evolution Modeling. Kluwer Academic/Plenum Publishers, New York.

Tucker, G.E., Slingerland, R., 1996. Predicting sediment flux from fold and thrust belts. Basin Res. 8, 329–349.

Upton, P., Craw, D., 2014. Extension and gold mineralisation in the hanging walls of active convergent continental shear zones. J. Struct. Geol. 64, 135–148.

Upton, P., Koons, P.O., Craw, D., Henderson, C.M., Enlow, R., 2009. Along-strike differences in the Southern Alps of New Zealand: consequences of inherited variation in rheology. Tectonics 28, 1–15.

Van Dissen, R., Yeats, R.S., 1991. Hope fault, Jordan thrust, and uplift of the Seaward Kaikoura Range, New Zealand. Geology 19, 393–396.

Walcott, R.C., Summerfield, M. a, 2008. Scale dependence of hypsometric integrals: an analysis of southeast African basins. Geomorphology 96, 174–186.

Willett, S., Beaumont, C., Fullsack, P., 1993. Mechanical model for the tectonics of doubly vergent compressional orogens. Geology 21, 371–374.

Willett, S.D., 1999. Orogeny and orography: The effects of erosion on the structure of mountain belts. J. Geophys. Res. 104, 28957–28981.

Williams, H., Hatcher, R., 1982. Suspect terranes and accretionary history of the Appalachian orogen. Geology 10, 530–536.

Wilson, C.K., Jones, C.H., Molnar, P., Sheehan, A.F., Boyd, O.S., 2004. Distributed deformation in the lower crust and upper mantle beneath a continental strike-slip fault zone: Marlborough fault system, South Island, New Zealand. Geology 32, 837.

Wilson, T.H., Dominic, J., 1998. Fractal interrelationships between topography and structure. Earth Surf. Process. Landf. 23, 509–525.

Wilt, N., 2013. The Cuda Handbook: A comprehensive Guide to GPU Programming. Pearson Education, Crawfordsville, Indiana.

Xu, T., Moore, I.D., Gallant, J.C., 1993. Fractals, fractal dimensions and landscapes — a review. Geomorphology 8, 245–262.

Zernitz, E., 1932. Drainage patterns and their significance. J. Geol. 40, 498–521.